Optimal focusing for maximal collection of entangled narrow-band photon pairs into single-mode fibers

Daniel Ljunggren* and Maria Tengner

Department of Microelectronics and Information Technology, The Royal Institute of Technology, KTH, Electrum 229,
SE-164 40 Kista, Sweden

We present a theoretical and experimental investigation of the emission characteristics and the flux of photon pairs generated by spontaneous parametric downconversion in quasi-phase matched bulk crystals for the use in quantum communication sources. We show that, by careful design, one can attain well defined modes close to the fundamental mode of optical fibers and obtain high coupling efficiencies also for bulk crystals, these being more easily aligned than crystal waveguides. We distinguish between singles coupling, γ_s and γ_i, conditional coincidence, $\mu_{i|s}$, and pair coupling, γ_c, and show how each of these parameters can be maximized by varying the focusing of the pump mode and the fiber-matched modes using standard optical elements. Specifically we analyze a periodically poled KTP-crystal pumped by a 532 nm laser creating photon pairs at 810 nm and 1550 nm. Numerical calculations lead to coupling efficiencies above 93% at optimal focusing, which is found by the geometrical relation L/z_R to be ≈ 1 to 2 for the pump mode and ≈ 2 to 3 for the fiber-modes, where L is the crystal length and z_R is the Rayleigh-range of the mode-profile. These results are independent on L. By showing that the single-mode bandwidth decreases $\propto 1/L$, we can therefore design the source to produce and couple narrow bandwidth photon pairs well into the fibers. Smaller bandwidth means both less chromatic dispersion for long propagation distances in fibers, and that telecom Bragg gratings can be utilized to compensate for broadened photon packets—a vital problem for time-multiplexed qubits. Longer crystals also yield an increase in fiber photon flux $\propto \sqrt{L}$, and so, assuming correct focusing, we can only see advantages using long crystals.

PACS number(s): 03.67.Mn, 03.67.Hk, 42.50.Dv, 42.65.Lm

I. INTRODUCTION

Spontaneous parametric downconversion (SPDC) accounts for the majority of entangled photon pairs being produced today. It can be described as a process in which the electromagnetic field of a single photon—traveling inside a dielectric material such as a birefringent crystal—interacts with the atoms by absorption and gives rise to a nonlinear response in the field of polarization, thereby leaving the possibility of two or more photons being re-emitted. The laws of conservation of energy and momentum, together with the randomness and indistinguishability in the process, also give rise to entanglement, a nonlocal correlation between the photons.

In quantum communication numerous experiments have been performed to date involving non-entangled or entangled photons being sent over long distances, e.g., sources of heralded single photons [1–3], quantum cryptography [4–6], and teleportation [7]. A typical such experiment involves launching each photon of a (entangled) pair into single-mode fibers and to deliver each one to a separate party for encoding or decoding. For successful distribution over long distances it is vital to have a high rate of pairs generated at the source, as the attenuation of the fiber is a strongly limiting factor even at the wavelength of 1550 nm for which the fiber is most transparent. Today, results with crystals of periodi-

cally poled materials have proved this viable even at moderate pump laser powers [8], and in some cases the problem has turned into a matter of limiting the pump power to avoid creating two pairs at the same time, as this will give false coincidences also when having low *single*-coupling efficiencies. Instead, what has gained importance is to have a high *pair*-coupling efficiency that increases the probability of both photons of a pair being present in the fibers once they have been created. Furthermore, the use of time-multiplexed schemes [9,10] have elicited the need of launching photons having very narrow frequency bandwidth and long coherence length in order to limit the effects of dispersion in the fibers, and to enable the use of interferometers. Rather than just filtering the emission at some desired width, as is commonly done, we will show that it is more efficient in terms of photon-rates to design the source so that the bandwidth is determined by the crystal length and fiber coupling alone.

It is the purpose of this article to calculate the maximum coupling efficiency achievable for photon pairs generated in crystals that are phase-matched for colinear emission in general, and for periodically poled KTiOPO$_4$ (PPKTP) crystals using non-degenerate quasi-phase matching (QPM) in particular. We look for the optimal condition for focusing of the pump onto the crystal and focusing of the emission onto the fiber-end (mode-matching) which maximizes either the single or the pair-coupling efficiency. The focusing is specified using the parameter $\xi = L/z_R$, adopted from [11] with a slight modification, where L is the length of the crystal and z_R is the Rayleigh range. We make no thin-crystal approximations, but take fully into account the focusing geometry of

*Corresponding author. Electronic address: daniellj@kth.se;
URL: http://www.quantum.se

all three interacting fields: pump, signal, and idler, by decomposing all three fields into a complete set of orthogonal plane-wave modes. Other optimizable parameters of these beams include the direction of the beam axis and the location of the focus. Both are regarded fixed, the former being motivated by the colinear geometry of perfect quasi-phase matching, and the latter by the fact that focusing onto the center of the crystal shows to give highest efficiencies. (Support for the last claim is given in [12] for second harmonic generation.) We also regard the center frequency of the beams, the power of the pump, and the optical properties of the crystal as fixed parameters of the problem. We take into account the polychromatic character of the emission but assume a monochromatic pump (continuous-wave pump), and we investigate how the coupling efficiency depends on the length of the crystal and the bandwidth of the wavelength filter in front of the fiber, but also how the fiber coupling affects the bandwidth of the coupled photons and the achievable photon-rates. Our goal is to give a simple recipe for setting up a colinear source of entangled photon pairs that optimizes the focusing for the highest single and pair coupling efficiencies into single mode fibers, and that also determines a suitable crystal length for a desired bandwidth.

Shortly after the demonstration of parametric generation (PG) and second harmonic generation (SHG) in the 1960s, Boyd and Kleinman [11], and others, addressed the focusing in non-colinear geometries of type-I and showed the importance of optimization for achieving maximal conversion efficiency in optical parametric oscillators and frequency doublers. By using cavities to enhance the processes one can control the spatial mode of the pump, signal and idler to support only the fundamental TEM$_{00}$ mode, and under this condition Boyd and Kleinman suggested that the general optimal focusing is to set the ξ-parameters of all fields the same ($\xi_p = \xi_s = \xi_i$). Later, Guha *et al.* [13] showed that having unequal parameters can improve the conversion even further and this is also supported by our results. The case of type-II SHG have also been studied [14], as well as sum- and difference frequency generation (SFG and DFG) [15], with similar results. These works were all treating the light as a classical field, having the signal beam acting as the relatively strong control-field that is being amplified by the much stronger pump-beam together with the creation of an idler. It is not unreasonable to expect that a different situation arises at the quantum level where both the signal and idler initially are in uncontrolled vacuum-states.

Spontaneous parametric downconversion commonly takes place in bulk crystal configurations where the signal and idler modes are not restricted by cavities. This will provide an additional degree of freedom. The pump is assumed to be TEM$_{00}$, but the emission will in general be spatially multi-mode. A central problem in this article is to find how much of the emission is in a transverse and longitudinal fundamental single-mode at different focusing conditions. For the transverse part, such a single-mode, being Gaussian shaped, is very close to the Bessel function of the first kind, $J_0(\alpha)$, which describes the shape of the fundamental fiber mode, and will therefore provide nearly perfect overlap. After determining the mode of the emission we also calculate the M^2 factor, commonly used as a measure of beam-quality, and

compare it to experimentally obtained results.

To our knowledge, no analysis has been made to date that characterizes the colinear emission in quasi-phase-matched materials in the way presented here, i.e., making no assumptions about short crystals or weak focusing. It should be noted that the analytical calculations become difficult without these assumptions and so our goal have been to formulate the final expression in such a way that it can be evaluated numerically with relative ease, with only simple assumptions being made. Taking into account all the needed degrees of freedom—azimuthal and polar angular spectrum and frequency included—these numerical computations will become quite time-consuming on an ordinary personal computer, but still doable.

Various other attempts have been made in the past to characterize the one- and two-photon spatial optical modes generated by non-colinear birefringent phase-matching. However, most of them do not use single-mode fibers to collect photons; Monken *et al.* [16] and Pittman *et al.* [17] show how focusing of the pump with a lens can increase the coincidence counts using an analysis limited to thin crystals, and Aichele *et al.* [18] seek to match the spatio-temporal mode of a conditionally prepared photon to a classical wave by spectrally and spatially filtering the trigger, however, without considering focusing effects.

More recent work connected to ours is a number of papers that consider the coupling into single-mode fibers; Kurtsiefer *et al.* [19] provide, for thin crystals, a hands-on method of determining the mode of the emission using the relation between the emission-angle and the wavelength coming from the phase-matching conditions. For maximal overlap between the emission mode and the fiber-matched mode (target) they presume it is best to choose the waist of the pump-mode and fiber-matched mode equal. According to [11], and our results, this is not optimal in general. Bovino *et al.* [20] take on a more sophisticated approach as they carry out the biphoton-state calculation for a non-colinear source, which takes into account focusing, dispersion, and walk-off and arrives at a closed expression for the coincidence efficiency. Other work have been continued along the same lines [21]; our conclusion from examining the formulas herein being that high efficiency can always be achieved for any length of crystal by choosing the pump waist large enough and the fiber-matched waist small enough. This is in contrary to our results which show an optimal value of the focusing parameter ($1 \lesssim \xi \lesssim 3$). Furthermore, as shown both in this report and in [11], for a specific crystal type and wavelength configuration the value of ξ is found to be a fixed constant for all crystal lengths which makes the pump-beam waist w_0 relate to the length as $w_0 \propto \sqrt{L}$ (at optimal focusing), while the results of Refs. [20,21] appear to show a linear relationship. We are not sure whether these apparent differences are best explained by the different situations of a non-colinear and colinear source, pulsed vs. continuous-wave pump, or by otherwise different models or parameters in either case. It can be noted that our results seem to provide good agreement with experiments.

The particular source of photon pairs that spurred the work of this article is presented by Pelton *et al.* in Ref. [22]. The main idea is to create polarization-entangled photon
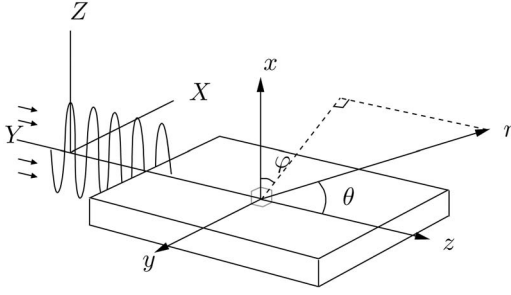
FIG. 1. The figure shows the periodically poled crystal with the laboratory coordinate system drawn. Also defined are the crystal's axes X, Y, and Z, referring to the polarization of the incoming and outgoing electromagnetic fields.

pairs at the non-degenerate wavelengths of 810 nm and 1550 nm from a pump-photon at 532 nm, using two orthogonally oriented [23], long, bulk KTP crystals. These crystals are periodically poled for quasi-phase matching which provides colinear emission suitable for coupling into single-mode fibers, but as told, also require some optimization for maximum throughput. Preliminary results can be found in [24]. Related work is found in [6,25,26].

The agenda of this article is as follows. Section II gives a mathematical background, starting in subsection II A with a review of the one and two-photon state of the emission derived in Appendix A. In Sec. II B we calculate the emitted modes, which are qualitatively measured using the beam quality parameter M^2. This is followed in subsection II C by a mathematical definition of the single-coupling, coincidence, and pair-coupling efficiencies. Section III presents the numerical results of the coupling (III A-III B), bandwidth (III C), and the M^2 factor (III D). Section IV covers the experimental setup and the experimental results, where a comparison is made to numerical predictions. Conclusions are found in Sec. V.

II. THEORETICAL DESCRIPTION

The aim of this section is to derive the formulas used for the numerical calculations of the emission modes, coupling efficiencies, and emission bandwidths for the emitted quantum state of the SPDC process, and also to give a physical meaning to these concepts in the role of single photon sources. We will optimize over the spatial parameters involved to find the highest quality modes and maximal coupling efficiencies attainable. The result is based on a calculation carried out in Appendix A involving the Hamiltonian that governs the interaction of spontaneous parametric down-conversion in quasi-phase-matched materials. The crystal is pumped by monochromatic and continuous wave laser light (p) of frequency ω_p, which is propagating in a Gaussian TEM_{00} mode along the z-axis, producing a signal (s) and idler (i) field in the same direction. Figure 1 defines the laboratory axes used; the z-axis being along the length L of the crystal, the x-axis along the height, and the y-axis along the width. The crystal is bi-axial, and the crystal axes X, Y, and Z are oriented as shown in the figure. We have chosen the

poling period in the crystal to allow for copolarized $(Z_p Z_s Z_i)$, colinear down-conversion, but the calculations are general enough to allow other polarization settings. The refractive indices, and thus the phase-matching, depends on the temperature of the crystal and is determined by the Sellmeier coefficients of PPKTP [27,28]. In general we are interested in phase-matching at non-degenerate wavelengths, and for such cases the shorter wavelength will be regarded as the signal and the longer wavelength as the idler.

Many references, following Klyshko [29], start with the coupled mode equations and look at the evolution of operators to find the two-photon state from SPDC in terms of a frequency and angular intensity distribution [30]. This is effectively the same as finding the diagonal elements of the second order moment density matrix which represent the incoherent part of the information of the state. This information is sufficient for determining the shape of the emission. However, it is not sufficient for determining the overlap between the emission and a single-mode fiber. In this case we need the "coherent" information available in the full density matrix. The approach we take in Appendix A and in the next subsection is to use the Schrödinger picture and look at evolution of the state to find the two-photon amplitude. In the following subsections we then diagonalize the corresponding density matrix into a sum of coherent parts (eigenmodes), and project each one onto the fiber-mode so that we can calculate the coupling efficiency as a sum of overlap coefficients. We also use this decomposition to calculate the electrical field and beam profile of the emission.

A. The emitted two-photon state

The two-photon amplitude describes the joint state of the signal and idler emission in terms of (internal) angular and frequency spectrum. Using spherical coordinates (see Fig. 1) the two-photon amplitude derived in Eq. (A28) becomes

$$
S(\epsilon, \theta_s, \theta_i, \Delta\varphi) = \frac{4\pi^2 \chi_2 f_1 L}{i\hbar} A^2(\epsilon)
$$
$$
\times \frac{k_p^Z w_{0p}}{\sqrt{2\pi}} e^{-(k_p^Z w_{0p})^2 [P^2 + Q^2]/4} \mathrm{sinc}\left[\frac{L}{2}\Delta k_z'\right],
$$
(1)

where, according to Eq. (A26)

$$
\Delta k_z' = k_s \cos\theta_s + k_i \cos\theta_i - k_p^Z \sqrt{1 - (P^2 + Q^2)} + K, \quad (2)
$$

and, according to Eq. (A25)

$$
P^2 + Q^2 = \frac{k_s^2 \sin^2\theta_s + k_i^2 \sin^2\theta_i + 2k_s k_i \sin\theta_s \sin\theta_i \cos(\Delta\varphi)}{(k_p^Z)^2}.
$$
(3)

All three interacting fields have been decomposed into a complete set of orthogonal plane-wave modes, $\boldsymbol{k}(\theta, \varphi)$. The magnitudes of the k-vectors, k_s and k_i, are given by Eq. (A17), θ_s and θ_i are the internal polar angles of the plane waves of signal and idler respectively, $\Delta\varphi$ is the difference in angle between the azimuthal angles φ_s and φ_i, and ϵ is the

frequency (specified by a single parameter due to exact energy-matching). Furthermore, χ_2 is the nonlinear coefficient of the crystal, K is the grating constant of the poling, L is the length of the crystal, and w_{0p} is the pump-beam waist radius. $A(\epsilon)$ is the frequency amplitude of the detector filter having a bandwidth $\Delta\lambda$ (FWHM) and a center wavelength λ_c (all wavelengths in vacuum). Via the relation $\epsilon = 2\pi c(n_\lambda/\lambda - n_{\lambda_c}/\lambda_c)$ its form, assuming a Gaussian shaped filter, is given by

$$A(\epsilon; \lambda) = e^{-2\log(2)(\lambda - \lambda_c)^2/\Delta\lambda^2}. \qquad (4)$$

In a plane wave mode-decomposition, Eq. (1) represents the two-photon field (that is generated in the crystal by the pump field) in the form of a continuous angular spectrum in polar and azimuthal degrees of freedom. Together with the frequency, the full state is a tensor-product of four degrees of freedom. We will need to discretize the spectrum in order to represent it on a computer. As the size of the Hilbert space of the full ket-vector becomes very large for a large number of points in resolution, we need to limit its size to make the numerical calculations feasible. In the following, the two-photon state is therefore explicitly represented only by the polar angles of the signal, $|\theta_s\rangle$, and the idler, $|\theta_i\rangle$, written as kets, leaving the state implicitly dependent upon the two remaining degrees of freedom, $\Delta\varphi$ and ϵ. The purpose of this notation is to reflect the actual way that the state is numerically implemented as a one-dimensional array of θ (the density matrix is a two-dimensional array), with separate arrays being calculated for each discrete value $\Delta\varphi$ and ϵ. Choosing N_θ discrete plane-wave modes as a basis of the polar angle, the two-photon state can then be formulated as

$$|\psi_{si}^{\Delta\varphi,\epsilon}\rangle = \sum_{m,n=1}^{N_\theta} S(\epsilon, \theta_s^{(m)}, \theta_i^{(n)}, \Delta\varphi)|\theta_s^{(m)}\rangle \otimes |\theta_i^{(n)}\rangle. \qquad (5)$$

There are a few approximations that have been made during the calculation of S, apart from the paraxial approximation inherent in the standard form of the angular spectrum representation of the Gaussian pump field of Eq. (A19). These include (i) the assumption of a constant pump k-vector magnitude $k_p = k_p^Z$ in order to remove the implicit dependence of θ_p and φ_p in Eq. (A16), which thus leads to Eq. (3), (ii) the assumption of an infinite coherence length of the pump (cw), providing a δ-function over frequency so that we can describe the signal and idler by a single frequency ϵ, and (iii) the assumption of having the same refractive indices along the crystal's X and Y axis, such that the X-component of the k-vectors can be set to the same as that of Y. The last assumption also provides a motivation for the output of completely rotationally symmetric modes, and will greatly simplify the expressions and the numerical calculations as the azimuthal angle dependence, via φ_s and φ_i, is automatically removed from the two-photon amplitude. The two-photon density matrix is given by

$$\rho_{si}^{\Delta\varphi,\epsilon} = |\psi_{si}^{\Delta\varphi,\epsilon}\rangle\langle\psi_{si}^{\Delta\varphi,\epsilon}|, \qquad (6)$$

which now contains four degrees of freedom; θ_s and θ_i being the two state parameters, and $\Delta\varphi$, ϵ being two other parameters which we will trace over later. Note that ρ_{si} is a descrip-

tion of the emission *inside* the crystal, not taking into account the refraction between crystal and air.

B. The emission modes and the beam quality, M^2

We are interested in the shape of the signal or idler beam profiles using free detection so that we can compare with images taken by a CCD camera. To do this comparison we need to have the beam described in terms of the electrical field, which is given as the Fourier transform of the angular spectrum (the density matrix). The electrical field, or intensity, then gives the beam profile which, in turn, determines the M^2 factor.

First, each signal or idler beam are made independent of the other beam by partially tracing over its partner. In the following we trace over the signal in the polar angle degree of freedom, and in doing so we get the reduced density matrix for the idler,

$$\rho_i^{\Delta\varphi,\epsilon} = \mathrm{Tr}_s(\rho_{si}^{\Delta\varphi,\epsilon}) = \sum_n^{N_\theta} \langle\theta_s^{(n)}|\rho_{si}^{\Delta\varphi,\epsilon}|\theta_s^{(n)}\rangle. \qquad (7)$$

The remaining dependence on $\Delta\varphi$ can also be removed following the standard trace-operation, which is here equivalent to a sum over density matrices,

$$\rho_i^\epsilon = \mathrm{Tr}_{\Delta\varphi}(\rho_i^{\Delta\varphi,\epsilon}) = \sum_m^{N_\varphi} \rho_i^{\Delta\varphi_m,\epsilon}. \qquad (8)$$

Additionally, as we could in principle measure the frequency of the photons at a resolution given by $\Delta\lambda_{res} = \lambda^2/c\Delta t_{gate}$ (set by the timing information of the detectors, >1 ns, to be <8 pm), which generally is much smaller than the bandwidths of the filters, we need to incoherently sum over the frequency ϵ in the same way, giving a final ρ_i describing the state of the idler,

$$\rho_i = \mathrm{Tr}_\epsilon(\rho_i^\epsilon) = \sum_n^{N_\epsilon} \rho_i^{\epsilon_n}. \qquad (9)$$

1. Mode decomposition

We cannot, however, directly now apply a Fourier transform to the reduced density matrix ρ_i, as it is generally mixed. Instead, we shall diagonalize ρ_i to find its eigenvectors and eigenvalues. For such a Hermitian matrix all eigenvalues are real and the eigenvectors will form a complete orthonormal set. Thence, the set will represent a natural mode-decomposition of the emission, and consequently, each vector, or mode, will represent a coherent part of the emission. The sum of all modes weighted by its corresponding eigenvalue will determine the state. For each such mode, on the other hand, we can apply a Fourier transform and thus find the electrical field modes. The squared sum of all electrical field modes, again weighed by the corresponding eigenvalue, will then determine the total electrical field. We will quantify this to show our future notation; the reduced density matrix is first diagonalized by $T^{-1}\rho T = D$, such that $T = (|\zeta_1\rangle, |\zeta_2\rangle, \dots, |\zeta_{N_\theta}\rangle)$ has the eigenvectors in the columns,
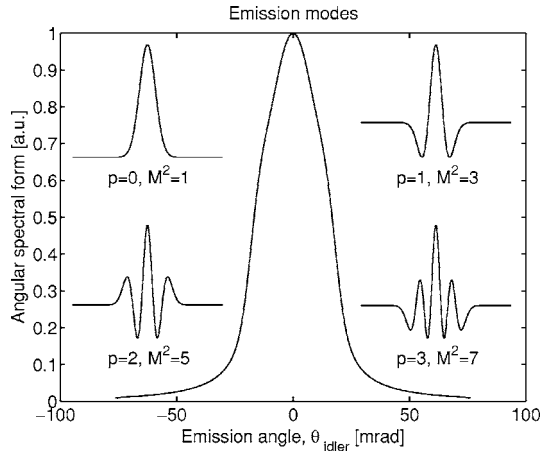
FIG. 2. The figure shows an example of the angular spectral form $u[\theta_y]$ of the emitted idler light att 1550 nm in a PPKTP crystal (central curve) which gives an M^2 factor less than 3 with a filter bandwidth $\Delta\lambda = 10$ nm. The pump at 532 nm is focused close to optimal, $\xi_p = 1.3$. The insets show the four lowest order LG_{p0} modes which are similar, but never the same as the natural eigenmodes of the emission, and illustrates how the M^2 factor in general grows with mode order.

and $\boldsymbol{D}$ has the eigenvalues λ_n in its diagonal elements. The result is a density matrix that can be represented as a sum of pure states,

$$\rho = \sum_{n=1}^{N_\theta} \lambda_n |\zeta_n\rangle\langle\zeta_n|, \tag{10}$$

where N_θ is the Hilbert-space dimension. Following this result, in Fig. 2 is plotted the one-dimensional angular spectral form $u[\theta_y]$, taken as an integration of the absolute square of the two-dimensional angular spectral amplitude $a_{xy}[\theta]$. We have $a_{xy}[\theta] = \sum_n \lambda_n \zeta_n[\theta]$, where $\zeta_n[\theta]$ is the discrete function representation of $|\zeta_n\rangle$, and $\theta^2 = \theta_x^2 + \theta_y^2$. Hence,

$$u[\theta_y] = \sum_{\theta_x} |a_{xy}[\sqrt{\theta_x^2 + \theta_y^2}]|^2, \tag{11}$$

is the one-dimensional angular spectral form.

2. The field intensity

We can now transform the angular spectrum modes $|\zeta_n\rangle$, into electrical field modes E_n. As these modes are rotationally symmetric and depend on one parameter only, the electrical field is most suitably expressed through the Hankel transform. In writing the transform in the following form we make use of the fact that the vector $|\zeta_n\rangle$, again written as a discrete function, $\zeta_n[\theta,\varphi] = \zeta_n[\theta]$, is independent of φ. Thus,

$$E_n(x,y,z) = \sum_\theta \lambda_n \zeta_n[\theta] e^{-ikz\cos\theta} J_0(k\sqrt{x^2+y^2}\,\theta), \tag{12}$$

where the basis functions $J_0(\alpha)$ of the Hankel transform are the Bessel function of zero order and the solution to $(1/2\pi)\int_0^{2\pi} \exp(i\alpha\cos\varphi)d\varphi$. However, the one-dimensional fast Hankel transform (FHT), which would possibly provide very fast computations, is not widely implemented, at least

not in an efficient form for use in Matlab or Mathematica and was not available to us at the time for the numerical calculations. Therefore, the next simplest transform at hand is the two-dimensional Fourier transform,

$$E_n(x,y,z) = \sum_\theta \sum_\varphi \lambda_n \zeta_n[\theta,\varphi] e^{-ikz\cos\theta}$$
$$\times e^{kx\sin\theta\cos\varphi} e^{ky\sin\theta\sin\varphi}. \tag{13}$$

With still two dimensions being used, Eq. (13) can also be rewritten using the polar angle components θ_x and θ_y,

$$E_n(x,y,z) = \sum_{\theta_x} \sum_{\theta_y} \lambda_n \zeta_n[\sqrt{\theta_x^2+\theta_y^2}] e^{-ikz\cos(\sqrt{\theta_x^2+\theta_y^2})}$$
$$\times e^{kx\sin\theta_x} e^{ky\sin\theta_y}, \tag{14}$$

where $\theta = \sqrt{\theta_x^2+\theta_y^2}$. In this form, which is the form we will use, Eq. (14) represents a standard single two-dimensional FFT. Note that this transform is, in general, not separable with respect to x and y into two, but simple, one-dimensional transforms. This is a characteristic of Laguerre-Gaussian modes and of the modes emitted by the crystal, in comparison to Hermite-Gaussian modes which are always separable.

The intensity is now given by incoherently summing all field-modes,

$$I(x,y,z) = \sum_{n=1}^{N_\theta} |E_n(x,y,z)|^2. \tag{15}$$

Finally, the transversely integrated intensity profile of the emitted beam is given by $I(y,z) = \sum_x I(x,y,z)$.

3. Gaussian beam fitting

The beam waist radius $w(z)$ can be found from the standard deviation $\sigma(z)$, or the second moment, of the intensity distribution $I(y,z)$, as $w(z) = 2\sigma(z)$, see Ref. [31]. The standard deviation is known to provide the correct waist estimate for arbitrary multimode light as opposed to trying to make a curve-fit with various mode-shapes. Readily, $\sigma^2(z) = \sum_y(y - \bar{y}(z))^2 I(y,z)$, where $\bar{y}(z) = \sum_y yI(y,z)$ is the expectation value with respect to the spatial position y in the intensity distribution. As said, we will use the beam quality factor M^2 to quantify the emission. This factor is determined through the Rayleigh range

$$z_R = \frac{\pi w_0^2}{M^2 \lambda}, \tag{16}$$

entering the standard Gaussian beam formula

$$w_{\text{model}}(z) = w_0\sqrt{1 + \left(\frac{z-z_0}{z_R}\right)^2}. \tag{17}$$

By varying the parameters w_0 and M^2 we can make a curve-fitting of the model profile $w_{\text{model}}(z)$ to the actual beam profile $w(z)$, such that the M^2-factor is determined. Eq. (16) states that the diffraction limited fundamental Gaussian mode TEM_{00} has a beam quality factor of $M^2 = 1$. As a comparison, this factor increases for general higher order Laguerre-Gaussian modes LG_{pm} [32], defined by the radial
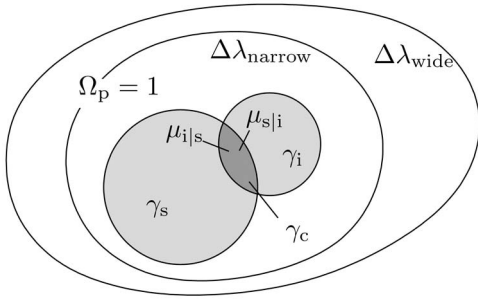
FIG. 3. The figure shows a Venn diagram. It illustrates the single coupling efficiencies γ_s and γ_i, pair coupling γ_c, and conditional coincidences $\mu_{s|i}$ and $\mu_{i|s}$, which are defined in the text. The total amount of pairs Ω_p generated within the bandwidth of the detector filter $\Delta\lambda$ is normalized to unity, and represents perfect coupling.

FIG. 4. The picture shows the geometry of focusing, with the Rayleigh-range z_R, the crystal length L, the beam waist radius w_0, and the focus offset z_0 being defined. The focusing parameter is defined as $\xi = L/z_R$.

index p and the azimuthal mode index $m=0$, such that $M^2 = 3$ for $p=1$, $M^2=5$ for $p=2$, and $M^2=7$ for $p=3$ and so on, see Fig. 2.

C. Single coupling, coincidence, and pair coupling

To characterize the source and to optimize the coupling of the emission into optical fibers we shall make use of three parameters: single coupling, conditional coincidence, and pair coupling. However, before we define each of the three coupling parameters we shall briefly comment on the necessity to relate them to the detection window being used, i.e., the frequency bandwidth of the detector filter $\Delta\lambda$. The emission will always fluoresce in a wide spectrum, and in that sense there is no meaning to speak about a coupling efficiency for photons that cannot be seen through the window in any case. By making a simple normalization to the filter bandwidth, the coupling probability will consistently measure only how well photons of specific frequencies are spatially collected into the fibers. For example, for any fixed filter and no spatial filtering, as is almost the case with a multimode fiber, and certainly the case in free-space, the coupling is always perfect. Effectively, this normalization enters the calculations through the bandwidth in Eq. (4). Figure 3 helps to illustrate the different coupling parameters using a Venn diagram.

1. Single coupling

The *single-coupling* efficiencies γ_s and γ_i are readily defined as the probability to find a photon in the fiber which has been emitted within a certain filter bandwidth. The single-coupling efficiency is useful when maximizing the individual rate of photons present in the fibers. To calculate the probability we shall take the overlap of the emitted modes with the mode of the fiber as seen from the crystal, here called the *fiber-matched mode*. That is to say, the form of the mode that can be traced back to the crystal from the fiber tip, not worrying about crystal refraction or any other optics in between performing the actual transformation. Also, we do not consider any additional aperture limitations enforced, e.g., by irises.

The true mode of the fiber is described by a Bessel function. However, it can be approximated very well with a fun-
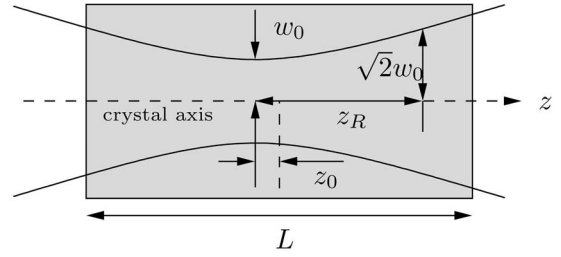
damental Gaussian which in normalized form is described by

$$|G_{00}\rangle = \frac{k^Z w_{00}}{\sqrt{2\pi}} e^{-ik^Z z_{00}\cos(\theta)-(k^Z w_{00})^2\sin^2(\theta)/4}|\theta\rangle, \qquad (18)$$

where w_{00} is the beam waist radius of the fiber-matched mode, TEM$_{00}$, as determined by the focusing system, and z_{00} is the location of the corresponding focus (which shall be at the center of the crystal $z_{00}=0$ for optimum coupling), see Fig. 4.

The single-coupling efficiency is trivially given by $\gamma = \mathrm{Tr}(|G_{00}\rangle\langle G_{00}|\rho)$, but the numerical optimization converges slowly and badly using this form. For this reason we shall exploit the diagonalization and calculate the single coupling efficiency as the sum of the projection of each emitted mode $|\zeta_n\rangle$ onto the fiber-matched mode $|G_{00}\rangle$,

$$\gamma = \sum_{n=1}^{N_\theta} \lambda_n |\langle\zeta_n|G_{00}\rangle|^2, \qquad (19)$$

where $|\zeta_n\rangle$ is given by the density matrix, ρ_s or ρ_i, as defined by Eq. (10), resulting in γ_s or γ_i respectively.

2. Optimization

The maximum achievable coupling efficiency is determined by an optimization of Eq. (19) with respect to the focusing conditions of either the pump mode, or the fiber-matched signal/idler mode, or both. To quantify the focusing we shall use the beam focusing parameter $\xi = L/z_R$, where L is the length of the crystal and z_R is the Rayleigh-range (note that we have $M^2=1$ for both the pump mode and the fiber-matched modes). See Fig. 4. The parameter is suitable as a dimensionless representation of the focusing geometry. (As will be shown further ahead, the results indeed show that the geometry is kept intact at optimal focusing, irrespectively of the length of the crystal, which corresponds to a fixed ξ^{opt}). In both Eq. (1) and Eq. (18) the parameter ξ enters through the beam waist radius of the pump mode w_{0p} and the signal/idler fiber-matched mode w_{00}, according to $w_{0p}=\sqrt{L\lambda_p/\pi\xi_p}$, and $w_{00}=\sqrt{L\lambda_{s,i}/\pi\xi_{s,i}}$. We can formalize the optimization of the signal and idler fiber-matched modes as

$$\gamma^{opt} = \max_{\xi_{s,i}} \gamma(\xi_p, \xi_{s,i}), \qquad (20a)$$

$$\xi^{\text{opt}} = \arg \max_{\xi_{\text{s,i}}} \gamma(\xi_{\text{p}}, \xi_{\text{s,i}}), \qquad (20b)$$

with γ given by Eq. (19).

3. Conditional coincidence

The *conditional coincidences*, $\mu_{\text{s|i}}$ and $\mu_{\text{i|s}}$ are useful for the characterization of heralded single photon sources, and are defined as the probability to find a photon in either the signal or the idler fiber given that the partner photon has entered its fiber, whether or not its detected. The conditional coincidence probability is found by first projecting the two-photon amplitude onto the one fiber, and then calculating the overlap with the other fiber in the same way as for single coupling. In this example we will search for $\mu_{\text{i|s}}$ and make a conditional measurement on the signal, defined by the following operator

$$M_{\text{s}} = |G_{00}^{(\text{s})}\rangle\langle G_{00}^{(\text{s})}|. \qquad (21)$$

Due to the measurement, the derivation of ρ_{i} will be slightly different here, and we need to take a few steps back and reformulate the two-photon density matrix $\rho_{\text{si}}^{\epsilon}$ as a coherent sum of amplitudes with respect to $\Delta\varphi$, instead of as a incoherent trace operation in Eq. (8). The density matrix is now written

$$\rho_{\text{si}}^{\epsilon} = \sum_m \sum_l |\psi_{\text{si}}^{\Delta\varphi_m,\epsilon}\rangle\langle\psi_{\text{si}}^{\Delta\varphi_l,\epsilon}|. \qquad (22)$$

Using the measurement operator M_{s}, the two-photon density matrix after the projection becomes

$$\rho_{\text{si|s}}^{\epsilon} = \frac{M_{\text{s}} \otimes \mathbb{1}_{\text{i}} \rho_{\text{si}}^{\epsilon} M_{\text{s}} \otimes \mathbb{1}_{\text{i}}}{\text{Tr}(M_{\text{s}} \otimes \mathbb{1}_{\text{i}} \rho_{\text{si}}^{\epsilon} M_{\text{s}} \otimes \mathbb{1}_{\text{i}})}. \qquad (23)$$

The reduced density matrix is readily found by tracing over the partner, $\rho_{\text{i|s}}^{\epsilon} = \text{Tr}_{\text{s}}(\rho_{\text{si|s}}^{\epsilon})$, which leaves only a trace over frequency, $\rho_{\text{i|s}} = \Sigma_n \rho_{\text{i|s}}^{\epsilon n}$. The conditional coincidence is now defined in the same way as for single coupling; we can replace γ by $\mu_{\text{i|s}}$ in Eq. (19), still using Eq. (10) to find the eigenvalues λ_n and eigenmodes $|\zeta_n\rangle$ of $\rho_{\text{i|s}}$. We have,

$$\mu_{\text{i|s}} = \sum_{n=1}^{N_\theta} \lambda_n |\langle\zeta_n|G_{00}^{(\text{i})}\rangle|^2, \qquad (24)$$

where $|G_{00}^{(\text{i})}\rangle$ is the fiber-matched mode of the idler. The parameter $\mu_{\text{s|i}}$ follows accordingly, as well as the formal optimization:

$$\mu^{\text{opt}} = \max_{\xi_{\text{s,i}}} \mu(\xi_{\text{p}}, \xi_{\text{s,i}}), \qquad (25a)$$

$$\xi^{\text{opt}} = \arg \max_{\xi_{\text{s,i}}} \mu(\xi_{\text{p}}, \xi_{\text{s,i}}). \qquad (25b)$$

4. Pair coupling

Finally, the *pair-coupling* efficiency γ_{c} is defined as the probability to find both photons of a pair in the respective fiber. This measure tells what fraction of the pairs enters the fibers compared to the total amount of pairs that are gener-

ated within the frequency bandwidth window. The pair-coupling can be derived from the single coupling and conditional coincidence using effectively Bayes's rule, see Fig. 3,

$$\gamma_{\text{c}} = \mu_{\text{i|s}}\gamma_{\text{s}} = \mu_{\text{s|i}}\gamma_{\text{i}}. \qquad (26)$$

The alternative is to calculate the coupling via $\gamma_{\text{c}} = \text{Tr}(M_{\text{s}} \otimes M_{\text{i}}\rho_{\text{si}})$, but this requires the calculation of ρ_{si}, which is computationally more demanding. When computing $\mu_{\text{i|s}}$ and γ_{s} via Eq. (26), using Eq. (24) and Eq. (19), the ket is sufficient, because we can simplify the trace-operation of Eq. (7), and also the projection of Eq. (23), to work in ket-space before the trace over frequency; $\rho_{\text{i}}^{\epsilon} = \text{Tr}_{\text{s}}(\rho_{\text{si}}^{\epsilon}) = \Sigma_{m,n,j} S_{m,j}S_{n,j}^* |\theta_{\text{i}}^{(m)}\rangle\langle\theta_{\text{i}}^{(n)}|$. We could also think of rewriting $\text{Tr}(M_{\text{s}} \otimes M_{\text{i}}\rho_{\text{si}})$ using two-photon kets in the same way, but as ρ_{si} generally becomes a mixture after tracing over frequency this is not an option. To compute γ_{c} before the frequency trace is also not an option numerically, as the trace over frequency involves a for-loop and optimization performed within it will reduce efficiency heavily.

The measure γ_{c} should be compared to $\eta \equiv \gamma_{\text{c}}/\sqrt{\gamma_{\text{s}}\gamma_{\text{i}}} = \sqrt{\mu_{\text{s|i}}\mu_{\text{i|s}}}$, which is basically γ_{c} normalized to γ_{s} and γ_{i}, that have been used by some authors [20,21]. The parameter η is useful as a type of measure of correlation that tells how well the focusing system has been set up to couple the modes of the idler emission to the same as those conditioned by the signal emission, or vice versa, depending on which of the two possess the smaller single-coupling efficiency. We intend to simply plot γ_{c} as this compares directly to γ_{s} and γ_{i} in terms of achievable photon rates; in principle, γ_{c} could be low while η is high.

III. NUMERICAL PREDICTIONS

All results in this section are for the case of a PPKTP crystal with the poling period $\Lambda = 2\pi/K = 9.6~\mu\text{m}$ operating at perfect quasi-phase matching; the pump at 532 nm creates emission at 810 nm and 1550 nm in the absolute forward direction. The temperature $T = 111~°\text{C}$, which affects the k-vector magnitudes, is chosen such that $k_{\text{p}} = k_{\text{s}} + k_{\text{i}} + K$, see Ref. [22].

The numerical calculations are implemented in Matlab using Eq. (1)–(3). All refractive indices are determined by the Sellmeier equations [27,28], setting the wavelength and temperature dependence of the k-vector magnitudes. The resolution N_θ of the discrete angular spectral amplitude representation in the polar degree are a few hundred points and varies between $1–100~\mu\text{radians}$, with the higher resolution for short crystals and strong focusing (wide-spread emission) and the lower resolution for long crystals and weak focusing (narrow emission). The needed azimuthal angle resolution N_φ is found to be $\gtrsim N_\theta/5$, and the frequency resolution N_ϵ varies between a few points for short crystals to a few hundred points for long crystals where the spectrally induced contribution to spatial multimode is larger. To spare the computer from unnecessary workload we observe that the two-photon density-matrix in Eq. (6) (scaling as N_θ^2 number of points in size) is always pure and can be fully represented by its amplitude vector alone (scaling as N_θ), for all of the calculations.

A. Single coupling

As said earlier, according to our definition the single-coupling efficiency depends on the emission bandwidth filter that is being used. This is because of the fact that many of the different frequencies created in the SPDC process will not couple into a single-mode fiber. Looking at a single frequency of the emission, the angular spectrum of the emission will be described by a single sinc-function for each of the plane waves of the pump, see Eq. (1). As will be argued in the next subsection, most of these sinc-functions will overlap nearly perfectly at optimal pump-focusing such that the emission is strongly spatially coherent and define almost a single-mode that will couple well into a single-mode fiber. If the pump-focusing is too weak it will create transverse multimode emission, as the many sinc-functions are then distributed along the transverse position of the pump beam and do not coincide. If the pump is instead focused too strongly the effect is the same, except that the multimode now originates from longitudinal position, also providing bad coupling. This is the general picture using the window of a single emission frequency.

If we look at a wide spectrum of the emission, each of the different frequencies can be seen as composed by a set of sinc-functions, each set in a different direction, and with every sinc in a set coming from one plane wave in the decomposition of the pump. For long crystals, when the width of the sinc-functions narrows down, the different sets of sinc-functions will no longer overlap. Within each set the sinc-functions are spatially well overlapping, thus defining a coherent single-mode, but as the sets do not overlap the emission will become spectrally multimode similar to above, also resulting in spatial multimode. This again provides poor coupling efficiencies. However, coupling into fibers automatically does some spatial filtering as it selects only the coherent part of the emission defining a single-mode, i.e., sinc-functions largely overlapping, and thereby it also does some frequency filtering. Altogether, this motivates why we have looked at only a single frequency of the emission for the results of the numerical calculations of the single coupling efficiencies shown in Figs. 5–7. We will refer to this case by saying that we have a "narrow enough" filter bandwidth, $\Delta\lambda_{narrow}$, which maintains a single-mode at optimal focusing of the pump and the signal and idler fibers, i.e. the bandwidth is narrow enough that the different sinc-sets, corresponding to different frequencies, within the bandwidth overlap (are coherent). Frequency filtering effects, as those just described, are left to the next section.

Figure 5 shows the single-coupling efficiency of the idler γ_i plotted against the crystal length L and the focusing of the pump-beam, via its waist w_{0p}. For each sample in the plot, the idler fiber focusing has been optimized using Eq. (20) to find the maximum coupling γ_i^{opt}. As seen, there is always the same maximal coupling to be found for any length of the crystal by changing the pump-beam waist radius accordingly. The straight lines show that the focusing parameters of both the pump ξ_p and the idler fiber focusing ξ_i^{opt} are constant, which means that the geometry of the beam profile and the crystal edges should stay fixed for different lengths of the crystal for optimal focusing. The said graph would look
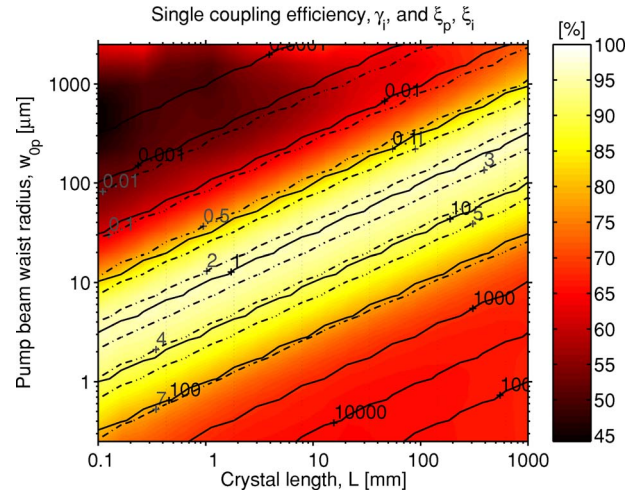

FIG. 5. (Color online) The single coupling of the idler γ_i^{opt}, plotted for a narrow enough filter bandwidth, $\Delta\lambda_{narrow}$, which shows that about 95% of the emission can be coupled into a single-mode fiber at optimal focusing. The solid line shows the pump-focusing parameter ξ_p, and the dashed-dotted lines show the focusing of the idler's fiber-matched mode ξ_i^{opt}. For each data sample the idler focusing has been optimized for maximum coupling using Eq. (20).

nearly the same for the signal emission, and, taking a different view of the results, Fig. 6 clearly shows the importance of choosing the right combination of focusing for the pump and for the fibers. Interestingly, we observe that as long as the fiber focusing is matched to the pump focusing, for any given length of the crystal, then the coupling efficiency will reach >45% irrespectively of the pump focusing. This fact may very well explain the relatively high efficiency nevertheless achived in many fiber-based SPDC-setups for which the experimentalist perhaps have not worried about changing the pump's focusing, but rather solely the fiber coupling.

Figure 7 shows both the signal and idler coupling in a graph that is parametrized by the pump focusing. In each case the optimal fiber focusing is found, and plotted along
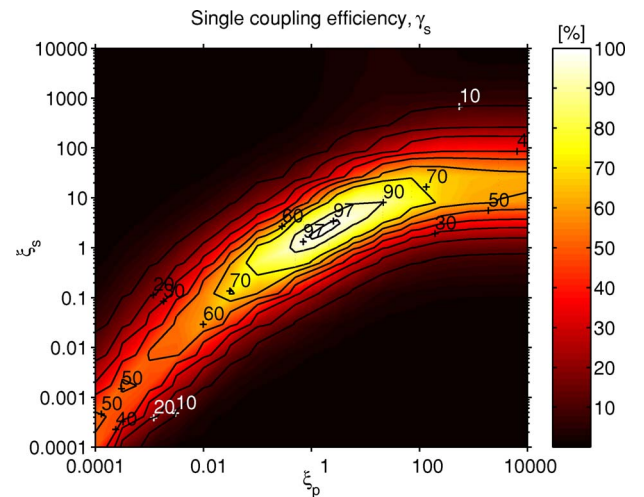

FIG. 6. (Color online) The single coupling of the signal γ_s, plotted for a narrow enough filter bandwidth, $\Delta\lambda_{narrow}$, which reaches a maximal 98% at optimal focusing, $\xi_p = 1.7$ and $\xi_s = 2.3$.

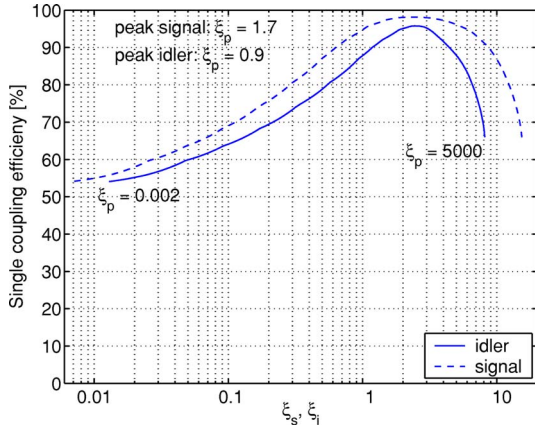FIG. 7. (Color online) The single couplings, γ_i^{opt} and γ_s^{opt}, reaches a maximum at $\xi_p=0.9$ for the idler, and at $\xi_p=1.7$ for the signal, which corresponds to $\xi_i^{opt}=2.4$ and $\xi_s^{opt}=2.3$. The line representing the signal in this graph is essentially a plot of the ridge of the surface in Fig. 6.

the horizontal axis. In this asymmetrical configuration it leads to a maximal $\gamma_s^{opt}=98\%$ when optimizing the focusing for the 810 nm emission ($\xi_p=1.7$ and $\xi_s^{opt}=2.3$), and $\gamma_i^{opt}=93\%$ for the 1550 nm emission ($\xi_p=0.9$ and $\xi_i^{opt}=2.4$). The optimal focusing of the pump depends on the amount of non-degeneracy for each of the wavelengths, e.g., for the degenerate case (1064 nm) the optimal focusing is $\xi_p=1.4$ and $\xi_{s,i}^{opt}=2.3$. It should be noted that, in general, the found optimal focusing parameters do not correspond to a match of the beam-waist sizes [19], but rather to an equal geometry. However, a matching of the waists are within the same order of magnitude comparable to using optimal focusing parameters.

B. Coincidence and pair coupling

For any focusing of the pump-beam, the fundamental modes of the signal and idler emission will be highly correlated, meaning that, e.g., a signal photon that enters its fiber will have its idler partner entering the other fiber, provided correct fiber focusing. At optimal focusing of the pump-beam, this correlation is always high if the partner beam is focused optimally, independent of the focusing of the beam that we condition upon. In other words, at optimal focusing of the pump-beam the conditional coincidence $\mu_{i|s}$, i.e., the probability of having the idler photon in the fiber given that the signal photon is in the fiber, will be mainly set only by its single coupling probability γ_i, which is always at a high value at optimal focusing due to the emission being mostly single-mode, see Fig. 8. In contrast, because of the multi-mode character of the emission at other pump-beam focusing settings than optimal, a high conditional coincidence can, in that case, only be attained near optimal focusing for both the signal and idler fibers. Each sample in the plot has been generated using Eq. (25) with a narrow filter, $\Delta\lambda_{narrow}$, at the signal side, as defined earlier, and without a filter at the idler side, when finding the maximum $\mu_{i|s}^{opt}$ that corresponds to optimal focusing of the idler, ξ_i^{opt}. As can be deduced from
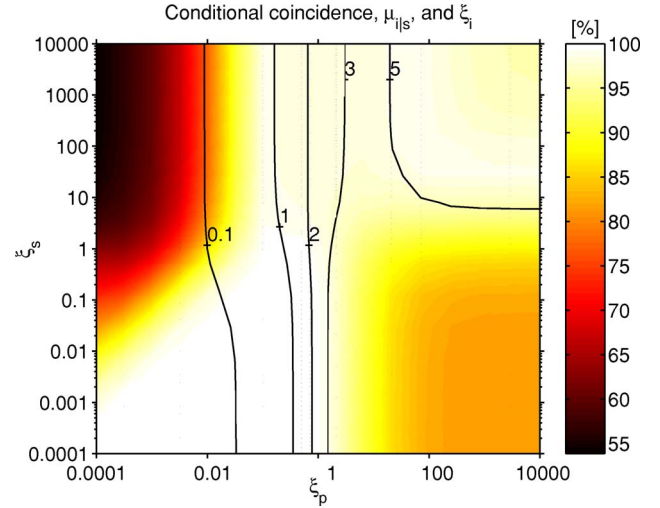

FIG. 8. (Color online) The conditional coincidence $\mu_{i|s}$, plotted versus the focusing of the pump ξ_p and the focusing of the signal's fiber-matched mode ξ_s. For each sample in the graph the focusing of the idler (ξ_i^{opt}=solid lines) is optimized to find the maximum $\mu_{i|s}^{opt}$ (up to 100%), using Eq. (25) with a narrow signal filter, $\Delta\lambda_{narrow}$, and no idler filter.

the graph, the conditional coincidence is always very high, reaching 100% for most weaker focusing conditions. When instead using an idler frequency filter that is matched to the signal filter, then $\mu_{i|s}$ will be bounded above by 71%, assuming Gaussian shaped filters on both sides. This limitation follows from the fact that while the signal photon of a given pair may very well be transmitted through its filter, the idler may not. Using Eq. (4), the maximum number can be easily derived from the normalized overlap integral $\int|A_s(\epsilon)|^2|A_i(\epsilon)|^2d\epsilon/\int|A_s(\epsilon)|^2d\epsilon=1/\sqrt{2}$, for which we note that the result is independent of the bandwidth.

Additional qualitative results on the optimal joint focusing can be found by turning to the pair coupling efficiency γ_c. As opposed to $\mu_{i|s}$, this measure relates to the total amount of pairs that is generated, and not only to those conditioned upon. As shown in Fig. 9, for optimal pump-beam focusing, there is a maximal value of about 97% for γ_c at $\xi_s=2.0$ and $\xi_i=2.3$. Note that, since the optimal pump-beam focusing varies for each of the beams for a non-degenerate wavelength case ($\xi_p=1.7$ for signal and $\xi_p=0.9$ for idler), we had to find a compromise using $\xi_p=1.3$. This graph is again plotted using a narrow filter at the signal and no filter at the idler. Equation (26) tells us that for matched filters, γ_c will also be limited to 71%, as long as $\gamma_s=1$ which is achievable with narrow filters. In general, both the conditional coincidence and the pair coupling decrease for wide bandwidths; $\mu_{i|s}$ in such case being bounded above by 100% and γ_c bounded above by the value of γ_s.

In terms of sources of heralded single photons, these results imply that almost perfect correlation can be achieved by careful focusing and by having no limiting interference filter on the triggered photon side; leaving such sources limited entirely by the transmission imperfections of lenses and filters, and by detector efficiencies.
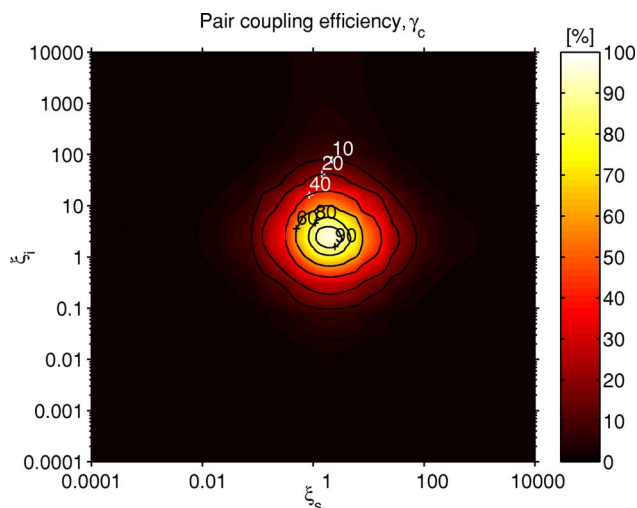
FIG. 9. (Color online) The pair coupling $\gamma_c = \mu_{i|s}\gamma_s$ at a pump focusing of $\xi_p = 1.3$, which is trade-off between what is optimal for the signal ($\xi_p = 1.7$) and the idler ($\xi_p = 0.9$) individually. At optimal focusing, $\xi_s = 2.0$ and $\xi_i = 2.3$, the maximum γ_c is about 97%, using a narrow signal filter, $\Delta\lambda_{narrow}$, and no idler filter.

C. Photon-rate and bandwidth

In this subsection we will look at the achievable photon fluxes in free-space and in single-mode fibers and its dependence on the crystal length. As we will argue, and we have shown numerically, this dependence will in turn depend on the chosen frequency filter. Our arguments will follow a series of steps, where the later steps include the effects of spatial and spectral filtering. The final results are found in Fig. 10 and Fig. 11.

As a first step, imagine the pump beam to be a single plane wave that is perfectly phase-matched for a single fre-
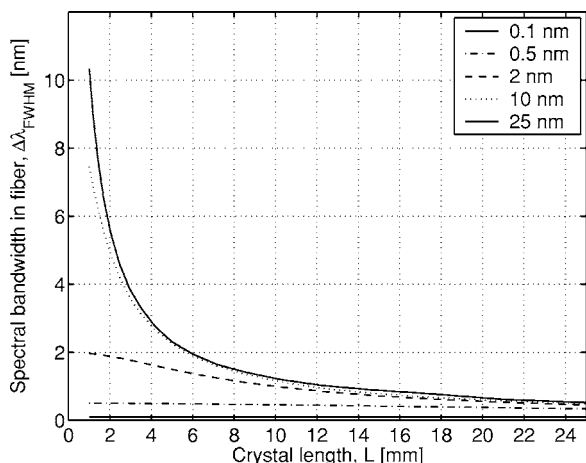

FIG. 10. The fiber coupled bandwidth is $\propto 1/L$ for a wide enough spectral filter $\Delta\lambda_{wide}$, see text, which can be said to be the case for the solid line of $\Delta\lambda = 25$ nm for all crystal lengths defined by the plot. In the limit of no filter at all, the graph corresponds to the single-mode bandwidth $\Delta\lambda_{SM}$, see Eq. (28). The graph shows the result for the signal emission (810 nm) at optimal focusing conditions, $\xi_p = 1.7$ and $\xi_s = 2.4$, and the legend shows what filter bandwidth $\Delta\lambda$ was used for each line.
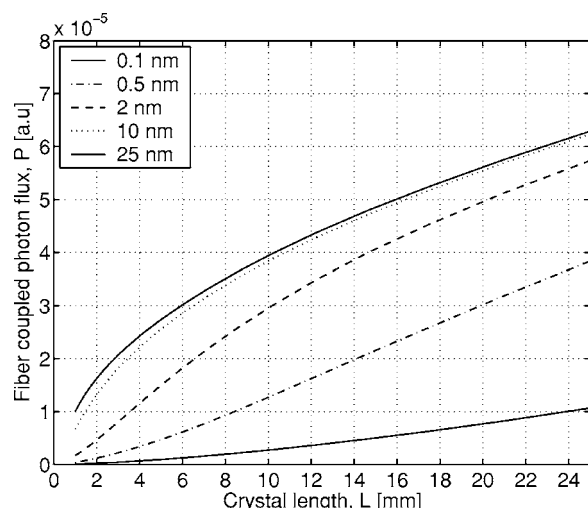

FIG. 11. The fiber photon flux is $\propto \sqrt{L}$ for a wide enough filter $\Delta\lambda_{wide}$, and $\propto L\sqrt{L}$ for a narrow enough filter $\Delta\lambda_{narrow}$. The filter is defined as narrow or wide in relation to the natural single-mode bandwidth $\Delta\lambda_{SM}$. For the solid line of $\Delta\lambda = 25$ nm the case has been reached where $\Delta\lambda = \Delta\lambda_{wide} > \Delta\lambda_{SM}$. The graph shows the result for the signal emission (810 nm) at optimal focusing conditions, $\xi_p = 1.7$ and $\xi_s = 2.4$, and the legend shows what filter bandwidth $\Delta\lambda$ was used for each line.

quency of the signal and the idler along the z-axis, called here the forward direction. In this case, by looking at the two-photon amplitude Eq. (1), we see that the height of the sinc-function, which describes the angular spectrum, is $\propto L$, corresponding to an L^2 dependence for the intensity (One should imagine two-dimensional, "Mexican-hat-like", sinc-functions). The width of the sinc will shrink $\propto 1/L$, such that the flux will increase $\propto L$. This argument is still valid considering the spatial transverse multimode emission created by such a plane wave pump, discussed earlier.

As a second step, consider a focused pump being composed of many differently directed plane waves. In this case, still looking at the same single frequency emitted, each such plane wave will phase-match a little less strongly than the one in the absolute forward direction. We will have a collection of sinc-functions being added together, each originating from a different plane pump wave, and numerical calculations show that the combined total width, or envelope, of these sinc-functions will decrease for longer crystals, thus adding to the previous result a factor $1/\sqrt{L}$, with the flux now becoming $\propto \sqrt{L}$.

The third step includes the observation that the energy of the pump beam is concentrated to the plane wave in the forward direction for longer crystals at optimal focusing. Equation (1) shows that the intensity will be $\propto w_{0p}^2$, because, at optimal focusing we have $z_R = L/\xi_p$, where z_R is given by Eq. (16), and thus $w_{0p}^2 \propto L$. The total flux is now $\propto L\sqrt{L}$.

As a last step we include filtering. In the previous steps we looked at a single frequency of the emission, which means that the bandwidth was narrow enough for the emission to be a single-mode (at optimal focusing). For narrow enough bandwidths we therefore get a flux

$$P \propto L\sqrt{L}\Delta\lambda_{\text{narrow}}, \qquad (27)$$

which is valid both in free-space and in fiber. As an effect of the phase-matching conditions there will be a tight connection between the spectral and spatial modes, as we described in Sec. III A for frequency filtering. In terms of fiber-coupling this means that when the fiber spatially filters the emission it will also effectively do frequency filtering. The bandwidth of the signal emission (810 nm) coupled into single-mode fibers (using no separate frequency filter) is given by

$$\Delta\lambda_{\text{SM}} = B/L, \qquad (28)$$

where the value $B = 1.23 \times 10^{-11} \, [\text{m}^2]$ is found for PPKTP when both the pump and fiber are focused optimally, see Fig. 10. We will refer to this bandwidth as the single-mode bandwidth. It will also determine how narrow the bandwidth of a filter ($\Delta\lambda_{\text{narrow}} < \Delta\lambda_{\text{SM}}$) need to be for any given length of the crystal to be considered narrow. The photon flux in the fiber will be

$$P \propto L\sqrt{L}\Delta\lambda_{\text{SM}} = \sqrt{L}, \qquad (29)$$

for any filter $\Delta\lambda > \Delta\lambda_{\text{SM}}$. In Fig. 11 we have plotted the flux for different filters, $\Delta\lambda_{\text{narrow}} < \Delta\lambda_{\text{SM}} < \Delta\lambda_{\text{wide}}$. For filter bandwidths that are "wide enough," $\Delta\lambda_{\text{wide}}$, the free-space emission will be multimode even at optimal pump focusing, and the free-space photon flux becomes

$$P \propto \sqrt{L}g(\Delta\lambda_{\text{wide}}), \qquad (30)$$

where g is some unknown and non-trivial function determined by the properties of the crystal material via the Sellmeier equations.

These results clearly show that it is advantageous to have long crystals as the photon-rate will always monotonically increase even when coupling the emission into single-mode fibers. As an effect, we can keep the pump power low, promoting the use of a compact and cheap laser. This requires that we change the focusing of both the pump ξ_p and the fibers $\xi_{s,i}$ to the optimal for some length L. Additionally, longer crystals give narrower bandwidth, which is very advantageous in many applications of entangled photons. For example, in time-multiplexed schemes it is crucial that the photon packets keep their widths in the fibers and do not broaden due to chromatic dispersion, and the broadening can be limited by having a narrow bandwidth. Another way of reducing the effect of broadening is by introducing negative dispersion using an appropriatly designed fiber Bragg grating. In general these have to be custom manufactured for broad bandwidths, but for telecom bandwidths, 30–80 GHz, (in the C-band, between 1525–1562 nm) these are standard off-the-shelf items, and corresponds to wavelength bandwidths of about 0.25–0.65 nm at 1550 nm. We can see from Eq. (28) that 70–180 mm long crystals are needed, taking into account the conversion factor between signal and idler bandwidths $[\Delta\lambda_i = (\lambda_{0i}/\lambda_{0p} - 1)^2 \Delta\lambda_s \approx 3.66 \times \Delta\lambda_s]$. Narrow bandwidth can of course be obtained by the use of spectral filters, however, our results show that it is better in terms of photon-rates to use long crystals to achieve small bandwidths rather than to strongly filter the emission of a short crystal.
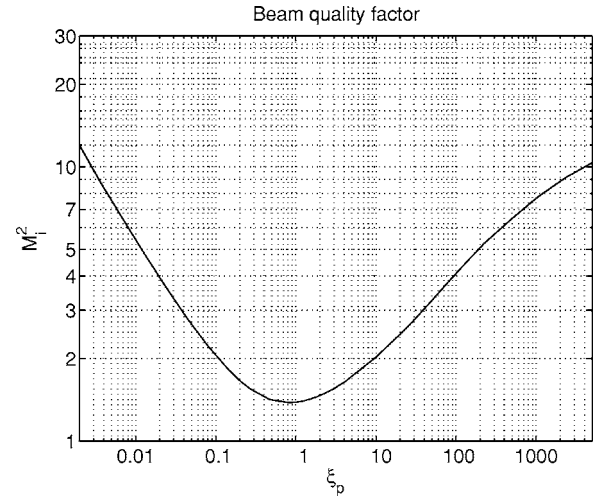

FIG. 12. The beam quality factor M^2 of the idler plotted against the pump beam focusing ξ_p. The smallest value, $M^2 = 1.4$, is found for $\xi_p = 0.9$

(This is in contrast to what is claimed by Lee *et al.* in Ref. [33], for birefringent phase-matching and intersecting cones.) Furthermore, with narrow bandwidth follows also long coherence length of the photons which is highly desirable when working with interferometry as is commonly done when using time-multiplexing analyzers to code and decode qubits.

D. M^2 and coupling

In this subsection we will present the numerical predictions of the emission mode in terms of the beam quality factor M^2 for different focusing conditions. We will also elaborate on the connection between the beam quality factor and the coupling efficiency.

Figure 12 shows the beam quality factor M_i^2 plotted against the focusing of the pump for a narrow enough frequency bandwidth of the idler emission ($\Delta\lambda_{\text{narrow}} \ll \Delta\lambda_{\text{SM}}$). There is a clear optimal focusing, where the emission reaches close to single-mode, $M_i^2 = 1.4$, at a focusing of $\xi_p = 0.9$. These results are valid for any length of the crystal, compare to Fig. 5. A low value of M^2 means that the light is close to a single-mode, and thus possible to couple well into a single-mode fiber. For bandwidths larger than the single-mode bandwidth $\Delta\lambda_{\text{wide}} \gg \Delta\lambda_{\text{SM}}$, the light will become spatially multimode and the coupling efficiency will decrease accordingly.

Figure 13 shows the relation between the coupling efficiency γ_i and the M_i^2, as the focusing ξ_p of the pump is varied. The correspondence is clear, and we can see that different M^2-values can provide the same coupling efficiency. This is so because the coupling efficiency is only determined by how much of the emission is in the fundamental mode. What determines the M^2 is the distribution of the light between the higher order modes, and this can differ from one case to another, even with the same amount contributing to the fundamental mode. In general, as we have said, too weak focusing will provide spatial transverse mul-
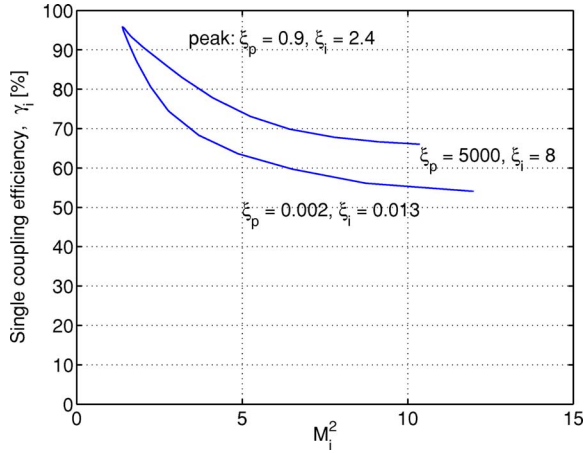
FIG. 13. (Color online) The single coupling γ_i versus the M^2 of the idler, using the same data as in Fig. 12 and Fig. 7. The graph is parametrized by the pump beam focusing and illustrate how a low M^2 is connected with a large γ_i.

timode, and too strong focusing will provide spatial longitudinal multimode. It can be deduced from Fig. 13 that longitudinal multimode, originating from too strong focusing, creates emission with relatively higher contribution to the fundamental mode for the same M^2 value.

IV. EXPERIMENTAL RESULTS

To verify some of the numerical results we compared with experiments. We have measured the beam quality factor, the bandwidth in the fiber, and the coupling efficiencies for different focusing conditions of the pump. The experimental setup is shown in Fig. 14. As a pump we use a frequency doubled YAG laser emitting approximately 60 mW in the TEM_{00} mode at 532 nm. Its M_p^2 value was measured to 1.06. After a band-pass filter (BP532), which removes any remaining infrared light, we "clean up" the polarization using a polarizing beam splitter (PBS). The polarization is controlled by a half wave plate (HWP) and a quarter wave plate (QWP) in front of the crystal. The pump-beam is focused onto the crystal using a achromatic doublet lens (f_p=50 mm) which introduces a minimal amount of aberrations not to destroy
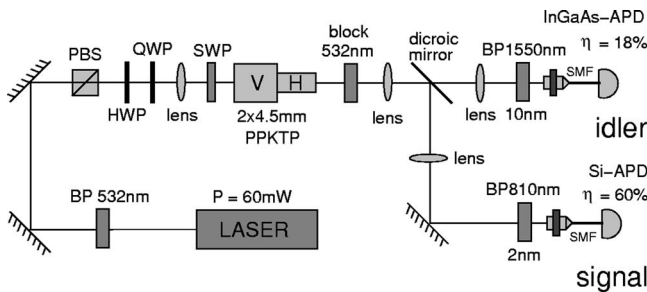

FIG. 14. The experimental setup used to create polarization entangled photon pairs, and to verify numerical results. PBS: polarizing beam splitter; HWP: half wave plate; QWP: quarter wave plate; SWP: short-pass filter; BP: band-pass filter; SMF: single-mode fiber; η: detection efficiency.

the low M^2 value. The QWP is set to undo any polarization ellipsitisation effects caused by the lens, and fluorescence caused by the same lens is removed by a Schott filter (KG5).

The next component is the crystal. This is a periodically poled, bulk 4.5 mm long KTP crystal, with a poling period of Λ=9.6 μm, which will colinearly create a signal at 810 nm and an idler at 1550 nm when heated in an oven to a temperature $T \approx 100°$. When the setup is used to create polarization entanglement, two crystals are present, one oriented for V and one for H, and the polarization of the pump is set to 45°. By coupling the emission from both crystals into single-mode fibers we cannot even in principle determine which crystal the photons came from, except by their polarization degree of freedom, and therefore the signal and idler will interfere in the diagonal basis and get entangled in polarization. This principle was first demonstrated by Kwiat *et al.* in Ref. [23]. Our first results was presented in Ref. [22], and the latest results, overcoming some problems of crystal dispersion and using optimal focusing, will be found in Ref. [34].

After the crystal, we block the pump light by a 532 nm band-stop filter, and the signal and idler emission is focused by achromatic doublet lenses. The rather small F-number ($F=f/D$, where f is the focal length and D is the beam diameter) of the emitted light ($F<40$ for f_p=50 mm and $F<9$ for f_p=12 mm) requires good quality lenses not to increase the M^2-factor. The lenses we use are all aberration free down to $F \approx 6-11$, and are also quite insensitive to an offset in the alignment of the optical axis.

To determine the coupling efficiencies and bandwidths, the complete setup of Fig. 14 was used. To separate the 810 nm and 1550 nm emission we used a dichroic mirror made for a 45° angle of incidence. The first lens (f_{si} =30 mm) is common to both signal and idler and its task is to refocus the beams somewhere near the dichroic mirror. The next two lenses (f_s=60 mm and f_i=40 mm) collimate each beam, and they are focused into the fiber-tips (with the mode field diameters being MFD_{810}=5.5 μm and MFD_{1550} =10.4 μm) using aspherical lenses with f=11 mm. In front of the fiber couplers we have first Schott filters (RG715) to block any remaining pump light, and then interference filters of 2 nm and 10 nm at the 810 nm and 1550 nm side respectively (BP). The detectors used were a Si-based APD (Perkin-Elmer SPCM-AQR-14) for 810 nm and a homemade $In_xGa_{1-x}As$-APD (Epitaxx) module for 1550 nm.

When determining the beam quality factor, M^2, we used only a single crystal oriented to create vertical (V) polarized light, and the complete setup of Fig. 14 was also not used. Instead, we focused the idler emission directly using a lens of focal length f_i=75 mm placed at a distance of 75 mm from the V-crystal to collimate the beam. At the additional distance of 470 mm we placed another lens with focal length f_i=150 mm that refocused the beam again, so that we could take measurements of the beam profile around its waist.

A. M^2 measurements, results

To obtain the results of Fig. 15 we first took images of the refocused idler beam in the x-y plane using an InGaAs-detector camera from Indigo Systems, model Alpha NIR.
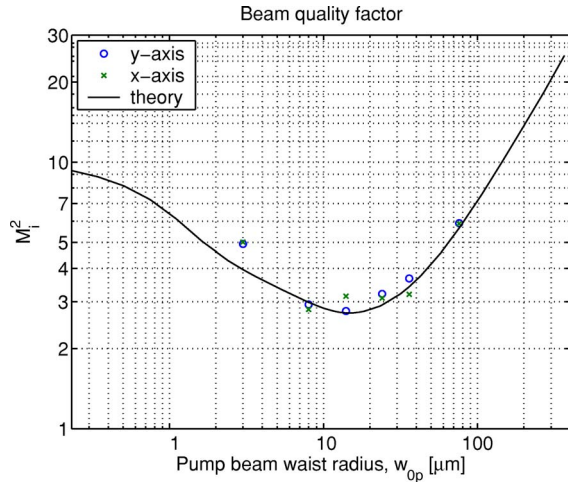
FIG. 15. (Color online) The experimentally observed beam quality factor, M_i^2, for the idler beam at different sizes of the pump beam waist radius w_{0p}. The lowest value of the M_i^2 is 2.8 at a 14 μm pump waist.

Several images were acquired for different positions along the z-axis around the waist, and we then integrated the resulting 2-dimensional surface over one axis to create an intensity profile for the remaining axis. Because of the detector noise we could not use the standard deviation method to find the beam radius, defined by the $1/e^2$ level. Instead we matched a Gaussian shaped function to the intensity profile to find the width. This is accurate enough for mode-shapes that are close to Gaussian, which is the case for low M^2 values. To limit the impact of the noise we applied a function that assigned greater weight to the center-values of the intensity profile. The widths of the beam for each z-axis position were then set together to find the beam profile of the emission, and its M^2 factor was determined by fitting to the standard Gaussian-beam function, Eq. (17). We now repeated the procedure for different focal lengths, f_p, of the pump lens: 12 mm, 30 mm, 50 mm, 75 mm, 100 mm, and 150 mm, each being placed at a distance that set the focus in the center of the crystal. The result, which is shown in Fig. 15, agrees fairly well with the numerical predictions. The shortest focal length lens, 12 mm, gave a somewhat higher M^2, which can be explained by the fact that this was the only singlet lens used, probably adding some aberrations, while the others where achromatic doublets. The lowest value, $M_i^2 = 2.8$, was found with the 50 mm lens giving a 14 μm pump waist radius w_{0p} inside the crystal, corresponding to $\xi_p = 2$ for the 4.5 mm long V-crystal (for later reference we observe that $\xi_p = 1.3$ for $L = 3$ mm agrees a little bit better with numerical results). Note that the M^2 values are slightly higher here compared to Fig. 12. This can be explained by the non-perfect phase-matching in the experimental case, resulting from either too low crystal temperature, uncertainty in the true value of the poling period (possibly deviating somewhat from its specification), or both.

B. Coupling efficiencies, results

The experimental data for the coupling efficiencies were obtained with the source producing polarization-

entanglement using two crystals. For this reason we expect the values to be a bit lower than predicted as we needed to focus the fiber-matched modes for both the H and the V crystal at the same time. We also have this problem with the pump beam, and we aimed at placing the focus at the intersecting faces of the two crystals for both the pump and the fiber. As already mentioned, the temperature of the crystal used in the experiment was set lower than required for absolute perfect phase matching at 810 nm and 1550 nm. This was because we observed higher photon fluxes at this setting. Contradictory as it may seem, the explanation is that the peak of the emission spectrum is not symmetrically centered around the above wavelengths, but rather towards $810 - \alpha$ and $1550 + \beta$, including a long tail representing the emission at larger angles. As our filters are centered for 810 nm and 1550 nm, the peaks of the emission can be moved to line up with these by changing the temperature, and thus the phase-matching, which will give somewhat higher fluxes although the coupling efficiencies will decrease according to our definitions. In addition to having a slightly wrong poling period these effects degrades the efficiencies, which we could verify numerically and which is supported by comparing Fig. 15 and Fig. 12. The obtained results for the single coupling efficiencies were $\gamma_s = 32\%$ and $\gamma_i = 79\%$, for the conditional coincidence $\mu_{i|s} = 34\%$, and for the pair coupling $\gamma_c = 11\%$, when focusing according to $\xi_p = 2.1$, $\xi_s = 3.2$, and $\xi_i = 2.5$ (as decided by available lenses, and assuming $L = 4.5$ mm). For these numbers we have compensated for the 35% transmission of the 1550 nm filter, and the 85% transmission of the 810 nm filter. The singles photon rate in the signal fiber was 2.3 Mcps (10^6 counts/sec) and in the idler fiber 2.4 Mcps. The total generated rate of photons before fiber coupling was estimated at 8.6 Mcps and the coincidence rate in the fibers was 274 kcps, (see Ref. [34]).

C. Bandwidth, results

We have used a spectrograph (SpectraPro 500i, ARC) to measure the bandwidth of the signal emission using the single-mode fiber without a filter. The bandwidth was 4 nm for the V-crystal and 6 nm for the H-crystal. Fig. 10 suggests that the effective length of the crystal being poled must be 3 mm and 2 mm respectively. Also, from Fig. 11, for the 2 nm filter, we can deduce that the 2 mm crystal should give roughly 55% of the photon rate of that of the 3 mm one. Experimental agreement is good, as we saw the H-crystal giving half the rate of the V-crystal (with no compensation done by balancing the fiber coupling or rotating the pump polarization). Referring again to Fig. 15 using the effective crystal length, the best pump beam focusing parameter is modified to $\xi_p = 1.3$ for $L = 3$ mm (V-crystal) which agrees roughly with the value of optimal focusing, $\xi_p = 0.9$.

V. CONCLUDING DISCUSSION

In summary, precise focusing of the pump-beam and the fiber-matched modes can significantly increase the coupling and coincidence efficiencies of quasi-phase matched SPDC-sources, which is important for applications needing highly

correlated pairs of single photons to propagate in fibers. We have shown how the beam quality factor of the emission changes with the focusing of the pump. At optimal focusing the emission is mostly created in a spatial single-mode, which couples well into single-mode fibers, and by maintaining a fixed geometry of the beam profile in relation to different lengths of the crystal this stays true for all lengths. We have also shown how the photon flux depends on the crystal length for different frequency filters, the conclusion being that longer crystals produce more photons per unit time at a smaller bandwidth.

In all of the calculations we have assumed a monochromatic (CW) pump laser. Looking for a possible extension to pulsed operation we observe that the interaction time, T, in Eq. (A18) for a CW laser is set by the coherence time of the pump alone, and as T is infinite it transforms into a delta-function of frequency in Eq. (A20). Using pulsed light, the integral $\int_0^T \exp(-i\Delta\omega t)$ should be replaced by $\int_{-\infty}^{\infty} h(t)\exp(-i\Delta\omega t)$, where $h(t)$ is the convolution, $h(t) = h_C(t) * h_L(t)$, between the form of the temporal wave-packet of the pump, $h_C(t)$, and the form of the crystal along the z-axis, $h_L(t)$. We observe that when $h_C(t)$ is narrow, like for pulsed operation, the transform of $h(t)$ will instead become a sinc-function, specifying an inexact energy-matching condition. Preliminary numerical calculations then show increased M^2-values and decreased coupling efficiencies. However, due to the characteristics of the convolution, it seems we can retain the good results of CW even for pulsed operation by using very long crystals, as this will bring back the delta-function at the limit of infinitely long crystals. For this discussion we have not yet worried about any dispersion effects that might come with long crystals and short pump pulses.

ACKNOWLEDGMENTS

APPENDIX A: THE TWO-PHOTON FREQUENCY AND ANGULAR SPECTRAL AMPLITUDE

The evolution of the number state vector is given by

$$|\psi\rangle = \exp\left[-i\frac{1}{\hbar}\int_{t_0}^{t_0+T} dt\hat{H}(t)\right]|\psi_{00}\rangle$$

$$\approx \left(\mathbb{1} + \frac{1}{i\hbar}\int_{t_0}^{t_0+T} dt\hat{H}(t)\right)|\psi_{00}\rangle, \quad \text{(A1)}$$

where $|\psi_{00}\rangle$ is the state at time t_0, T is the time of interaction, and $\hat{H}(t)$ is the Hamiltonian

$$\hat{H}(t) = \int_V \chi^{(2)}\hat{E}_p^{(+)}\hat{E}_s^{(-)}\hat{E}_i^{(-)}d^3r + \text{H.c.} \quad \text{(A2)}$$

There are three interacting fields in the crystal's volume V ignoring all higher-order terms ($n \geq 3$) of the nonlinearity $\chi^{(n)}$. All three fields have the same polarization (ZZZ):

$$E_p^{(+)} = \sum_{s_p} A_p(s_p)e^{i(k_p s_p \cdot r - \omega_p t + \phi_p)}, \quad \text{(A3a)}$$

$$\hat{E}_s^{(-)} = \int d\phi_s \int d\omega_s A(\omega_s)\sum_{s_s} e^{-i(k_s s_s \cdot r - \omega_s t + \phi_s)}\hat{a}_s^{\dagger}(\omega_s, s_s),$$
$$\text{(A3b)}$$

$$\hat{E}_i^{(-)} = \int d\phi_i \int d\omega_i A(\omega_i)\sum_{s_i} e^{-i(k_i s_i \cdot r - \omega_i t + \phi_i)}\hat{a}_i^{\dagger}(\omega_i, s_i).$$
$$\text{(A3c)}$$

The field of the pump is classical and monochromatic so that we can replace $\hat{E}_p^{(+)}$ by $E_p^{(+)}$. The plus-sign denotes conjugation, i.e., annihilation ($+$) or creation ($-$) of the state. In all the calculations we use the notation $k = ks$, where s is the unit length vector of k. The angular amplitude spectrum $A_p(s_p)$ takes into account the focusing of the pump. For signal and idler, we sum over both frequency and angular modes, where $\hat{a}(\omega, s)$ is the field operator, and $A(\omega)$ is the frequency amplitude of a Gaussian shaped detector filter having the bandwidth $\Delta\lambda$ (FWHM) and center wavelength λ_c (all wavelengths in vacuum). Via the relation $\omega = 2\pi c n_\lambda/\lambda$ its form is given by

$$A(\omega;\lambda) = e^{-2\log(2)(\lambda - \lambda_c)^2/\Delta\lambda^2}. \quad \text{(A4)}$$

Each signal and idler photon is created with a random phase, ϕ_s and ϕ_i respectively, which we also need to sum over. The only nonzero solution is completely correlated phases as will be shown later. The phase of the pump ϕ_p is constant but arbitrary.

For periodically poled materials, the nonlinearity $\chi^{(2)}$ has sharp boundaries, and later on in the calculations it will facilitate to make an expansion of $\chi^{(2)}$ into its Fourier-series components

$$\chi^{(2)} = \chi_2 f(r) = \chi_2 \sum_{m=0}^{\infty} f_m e^{-imK \cdot r}, \quad \text{(A5)}$$

and then do a sinusoidal approximation using the first term,

$$\chi^{(2)} = \chi_2 f_1 e^{-iK \cdot r}, \quad \text{(A6)}$$

where $K = 2\pi/\Lambda e_z$, and Λ is the grating period. Appendix B treats the case of a $M+1$ term series expansion.

From Eq. (A1) the number state becomes

$$|\psi\rangle = |\psi_{00}\rangle + \int\int d\omega_s d\omega_i \sum_{s_s}\sum_{s_i} S(\omega_s,\omega_i,s_s,s_i)\hat{a}_s^\dagger \hat{a}_i^\dagger |\psi_{00}\rangle$$

$$= |\psi_{00}\rangle + G_2|\psi_{11}\rangle, \tag{A7}$$

where G_2 is the unnormalized amplitude for the two-photon number state,

$$G_2 = \langle\psi_{11}|\psi\rangle = \int\int d\omega_s d\omega_i \sum_{s_s}\sum_{s_i} S(\omega_s,\omega_i,s_s,s_i), \tag{A8}$$

such that for $t_0=0$,

$$\frac{1}{i\hbar}\int_0^T dt\,\hat{H}(t) = G_2\hat{a}_s^\dagger \hat{a}_i^\dagger - \text{H.c.} \tag{A9}$$

Our goal now is to arrive at an expression for the amplitude S which will also enter in the state of frequency and angular spectrum of the form

$$|\psi_{\omega,s}\rangle = \int\int d\omega_s d\omega_i \sum_{s_s}\sum_{s_i} S(\omega_s,\omega_i,s_s,s_i)|\omega_s\rangle|\omega_i\rangle|s_s\rangle|s_i\rangle. \tag{A10}$$

We start by inserting Eq. (A6) into Eq. (A2) and then Eq. (A2) into Eq. (A9) which gives

$$G_2 = \frac{1}{i\hbar}\int_0^T dt\int_V d^3r\,\chi_2 f_1 e^{-iK\cdot r}E_p^{(+)}E_s^{(-)}E_i^{(-)}. \tag{A11}$$

By making a substitution of the fields in Eq. (A3) into Eq. (A11), and via identification using Eq. (A8) we find that

$$S(\omega_s,\omega_i,s_s,s_i) = \chi_2 f_1 A(\omega_s)A(\omega_i)\sum_{s_p} A_p(s_p)$$

$$\times \int_{-L/2}^{L/2} dz\int_{-\infty}^{\infty} dy\int_{-\infty}^{\infty} dx\,e^{-i\Delta k\cdot(xe_x+ye_y+ze_z)}$$

$$\times \frac{1}{i\hbar}\int_0^{2\pi}\int_0^{2\pi} d\phi_s d\phi_i\int_0^T dt$$

$$\times e^{-i[(\omega_s+\omega_i-\omega_p)t+\phi_s+\phi_i-\phi_p]}, \tag{A12}$$

where the volume integral has been expressed in a Cartesian coordinate system ($r=xe_x+ye_y+ze_z$, see Fig. 1),

$$\int_V d^3r = \int_{-L/2}^{L/2} dz\int_{-\infty}^{\infty} dy\int_{-\infty}^{\infty} dx. \tag{A13}$$

We have also introduced the phase mismatching vector

$$\Delta k = k_s s_s + k_i s_i - k_p s_p + K \tag{A14a}$$

$$= \Delta k_x e_x + \Delta k_y e_y + \Delta k_z e_z. \tag{A14b}$$

In a Cartesian coordinate system the normalized vectors s are represented by

$$s_s = p_s e_x + q_s e_y + m_s e_z,$$

$$s_i = p_i e_x + q_i e_y + m_i e_z,$$

$$s_p = p_p e_x + q_p e_y + m_p e_z,$$
$$\tag{A15}$$

$$K = Ke_z,$$

where p, q, and m are the normalized components of s in each of the three dimensions [30].

Because of the rotational symmetry of the emitted modes, it is suitable to use a spherical coordinate system (θ,φ), for which $p=\sin\theta\cos\varphi$, $q=\sin\theta\sin\varphi$, and $m=\cos\theta$. The phase-mismatch vector components then become

$$\Delta k_x = k_s\sin\theta_s\cos\varphi_s + k_i\sin\theta_i\cos\varphi_i - k_p\sin\theta_p\cos\varphi_p,$$

$$\Delta k_y = k_s\sin\theta_s\sin\varphi_s + k_i\sin\theta_i\sin\varphi_i - k_p\sin\theta_p\sin\varphi_p,$$

$$\Delta k_z = k_s\cos\theta_s + k_i\cos\theta_i - k_p\cos\theta_p + K. \tag{A16}$$

Note that the magnitude of the signal and idler k-vectors implicitly depends on the polar angle θ according to

$$k_s(\theta_s) = 1/\sqrt{\left(\frac{\cos\theta_s}{k_s^Z}\right)^2 + \left(\frac{\sin\theta_s}{k_s^Y}\right)^2}, \tag{A17a}$$

$$k_i(\theta_i) = 1/\sqrt{\left(\frac{\cos\theta_i}{k_i^Z}\right)^2 + \left(\frac{\sin\theta_i}{k_i^Y}\right)^2}, \tag{A17b}$$

where k_s^Z, k_s^Y, k_i^Z, and k_i^Y are the constant magnitude of the k-vectors along the crystals Z- and Y-axis, respectively (k_p need to be constant and equal to k_p^Z as we will soon show). Generally, there is negligible difference in refractive indices between the crystal's X and Y axes which cancels the dependence on the azimuthal angle φ in the equations above. We therefore use the Y axis as the major axis being orthogonal to Z.

Using spherical coordinates exclusively leads to

$$S(\omega_s,\omega_i,\theta_s,\theta_i,\varphi_s,\varphi_i)$$

$$= \chi_2 f_1 A(\omega_s)A(\omega_i)\int_0^{\pi/2}\sin\theta_p d\theta_p\int_0^{2\pi} d\varphi_p A_p(\theta_p,\varphi_p)$$

$$\times \int_{-L/2}^{L/2} dz\int_{-\infty}^{\infty} dy\int_{-\infty}^{\infty} dx\,e^{-i[\Delta k_x x+\Delta k_y y+\Delta k_z z]}$$

$$\times \frac{1}{i\hbar}\int_0^{2\pi}\int_0^{2\pi} d\phi_s d\phi_i\int_0^T dt\,e^{-i[(\omega_s+\omega_i-\omega_p)t+\phi_s+\phi_i-\phi_p]}. \tag{A18}$$

The angular spectral amplitude A_p of the pump beam in Eq. (A18) is Gaussian shaped for a laser emitting in a TEM_{00} single mode, and in spherical coordinates it becomes [30]

$$A_p(\theta_p,\varphi_p) = \frac{k_p w_{0p}}{\sqrt{2\pi}} e^{-(k_p w_{0p})^2\sin^2\theta_p/4}, \tag{A19}$$

where the beam waist radius w_{0p} of the focused pump beam has entered the calculations. The function is normalized to

represent the same constant power available in the beam at different focusing conditions.

Now we will solve the integrals over space, time, and phase in Eq. (A18). In doing so we note that there are three spatial integrals of which two are the Fourier transforms of unity (dx and dy) and one is the transform of a box-function (dz). The transforms turn into two δ-functions and a sinc-function respectively. The time-integral also turns into a δ-function of the three frequencies ω_s, ω_i, and ω_p. This is because we have a monochromatic pump-beam with infinite coherence length, which effectively leads to an infinite interaction-time, $T \to \infty$, even for short crystals. The two integrals over the random phases ϕ_s and ϕ_i will make the amplitude S vanish completely if the phases are not fully correlated with each other. Therefore, the only non-zero solution is when the two phases add up to a constant. S can be complex-valued, thus yielding the relation $\phi_s + \phi_i = \phi_p + C$. If we let $C = 0$ for simplicity, we are led to

$$S(\omega_s, \omega_i, \theta_s, \theta_i, \varphi_s, \varphi_i)$$

$$= \chi_2 f_1 A(\omega_s) A(\omega_i) \int_0^{\pi/2} \sin \theta_p d\theta_p \int_0^{2\pi} d\varphi_p A_p(\theta_p, \varphi_p)$$

$$\times \delta(\Delta k_x) \delta(\Delta k_y) L \, \text{sinc}\left[\frac{L}{2} \Delta k_z\right] \frac{4\pi^2}{i\hbar} \delta(\omega_s + \omega_i - \omega_p).$$

$$(A20)$$

We now have two integrals over θ_p and φ_p with δ-functions over Δk_x and Δk_y which in turn depends on θ_p and φ_p according to Eq. (A16). The integrals can be canceled in a few steps by setting the equalities $\Delta k_x = 0$ and $\Delta k_y = 0$, and to that end we need to assume that k_p is constant for small angles θ_p, i.e., $k_p = k_p^Z$ which we believe is a fair approximation for pump-light that is not extremely focused. By extreme we mean beyond the validity of the paraxial approximation. The latter equality applied to Eq. (A16) gives

$$\varphi_p' = \arcsin\left(\frac{k_s \sin \theta_s \sin \varphi_s + k_i \sin \theta_i \sin \varphi_i}{k_p^Z \sin \theta_p'}\right). \quad (A21)$$

Equation (A21) together with the relation $\arcsin(x) = \arccos(\sqrt{1-x^2})$ now gives the following expression for $\Delta k_x = 0$ of Eq. (A16) (with φ_p primed),

$$k_s \sin \theta_s \cos \varphi_s + k_i \sin \theta_i \cos \varphi_i$$

$$- k_p^Z \sin \theta_p' \sqrt{1 - \left(\frac{k_s \sin \theta_s \sin \varphi_s + k_i \sin \theta_i \sin \varphi_i}{k_p^Z \sin \theta_p'}\right)^2}$$

$$= 0. \quad (A22)$$

If we now take the square of Eq. (A22) and solve for θ_p' we get

$$\theta_p' = \arcsin \sqrt{P^2 + Q^2} = \arccos \sqrt{1 - (P^2 + Q^2)}, \quad (A23)$$

where

$$P = \frac{k_s \sin \theta_s \sin \varphi_s + k_i \sin \theta_i \sin \varphi_i}{k_p^Z}, \quad (A24a)$$

$$Q = \frac{k_s \sin \theta_s \cos \varphi_s + k_i \sin \theta_i \cos \varphi_i}{k_p^Z}. \quad (A24b)$$

Furthermore,

$$P^2 + Q^2 = \frac{k_s^2 \sin^2 \theta_s + k_i^2 \sin^2 \theta_i + 2k_s k_i \sin \theta_s \sin \theta_i \cos(\Delta\varphi)}{(k_p^Z)^2},$$

$$(A25)$$

where we are allowed to introduce $\Delta\varphi = \varphi_s - \varphi_i$. This is a result of the assumption of rotational symmetry and will lead to the final state being invariant to a common variation in the azimuthal angles for signal, φ_s, and idler, φ_i. As shown here, only the angle-difference is of importance. Using Eq. (A23) in the expression for Δk_z of Eq. (A16) we have

$$\Delta k_z' = k_s \cos \theta_s + k_i \cos \theta_i - k_p^Z \sqrt{1 - (P^2 + Q^2)} + K.$$

$$(A26)$$

At this stage the two integrals in Eq. (A20) have been canceled and the amplitude can be simplified as

$$S(\omega_s, \omega_i, \theta_s, \theta_i, \Delta\varphi) = \chi_2 f_1 A(\omega_s) A(\omega_i) A_p(\theta_p', \varphi_p')$$

$$\times L \, \text{sinc}\left[\frac{L}{2} \Delta k_z'\right] \frac{4\pi^2}{i\hbar} \delta(\omega_s + \omega_i - \omega_p).$$

$$(A27)$$

One further simplification includes the observation that the frequency δ-function can be reduced to unity by introducing a common frequency ϵ instead of ω_s and ω_i as defined by $\omega_s = \omega_{0s} + \epsilon$, $\omega_i = \omega_{0i} - \epsilon$, so that for two matched filters the form of the filter amplitude becomes squared. Using also Eq. (A23) together with Eq. (A19) the expression for the amplitude of the state of frequency and angular spectrum finally becomes

$$S(\epsilon, \theta_s, \theta_i, \Delta\varphi) = \frac{4\pi^2 \chi_2 f_1 L}{i\hbar} A^2(\epsilon) \frac{k_p^Z w_{0p}}{\sqrt{2\pi}} e^{-(k_p^Z w_{0p})^2 [P^2 + Q^2]/4}$$

$$\times \text{sinc}\left[\frac{L}{2}(k_s \cos \theta_s + k_i \cos \theta_i\right.$$

$$\left. - k_p^Z \sqrt{1 - (P^2 + Q^2)} + K)\right], \quad (A28)$$

where $P^2 + Q^2$ is defined by Eq. (A25) and the k_s's and k_i's by Eq. (A17).

We now have a final expression for the two-photon amplitude

$$G_2 = \int d\epsilon \int \int \sin \theta_s d\theta_s \sin \theta_i d\theta_i \int d\Delta\varphi S(\epsilon, \theta_s, \theta_i, \Delta\varphi),$$

$$(A29)$$

which gives the two-photon state-vector in terms of frequency and angular spectrum in the form of Eq. (A10)

$$|\psi_{\epsilon, \theta, \Delta\varphi}\rangle = G_2 |\epsilon\rangle |\theta_s\rangle |\theta_i\rangle |\Delta\varphi\rangle. \quad (A30)$$

APPENDIX B: SERIES EXPANSION OF $\chi^{(2)}$

The poling structure of periodically poled crystal has the approximate form of a square-function along the z-axis. In such a case, the $M+1$ term series expansion of $\chi^{(2)}$ become

$$\chi^{(2)} = \chi_2 f(\boldsymbol{r}) = \frac{4\chi_2}{\pi} \sum_{m=0}^{M} \frac{(-1)^m}{2m+1} e^{-i(2m+1)\boldsymbol{K}\cdot\boldsymbol{r}}, \quad \text{(B1)}$$

where $\boldsymbol{K} = 2\pi/\Lambda \boldsymbol{e}_z$, and Λ is the grating period. In the following expression we have isolated the z-dependent part of Eq. (A18):

$$\chi_2 f_1 \int_{-L/2}^{L/2} dz\, e^{-i\Delta k_z z}. \quad \text{(B2)}$$

Now, putting the series expansion of $\chi^{(2)}$ into the calculations of Appendix A, the former expression should be replaced by

$$\frac{4\chi_2}{\pi} \int_{-L/2}^{L/2} dz \sum_{m=0}^{M} \frac{(-1)^m}{2m+1} e^{-i\Delta k_z^{(m)} z}, \quad \text{(B3)}$$

where

$$\Delta k_z^{(m)} = \Delta k_z' + 2mK. \quad \text{(B4)}$$

By reversing the order of the sum and the integral in Eq. (B3) we can identify a Fourier transform of box-function with an extra phase. The result of the transform is a sinc, providing thus

$$\frac{4\chi_2}{\pi} \sum_{m=0}^{M} \frac{(-1)^m}{2m+1} \text{sinc}\left[\frac{L}{2}(\Delta k_z' + 2mK)\right], \quad \text{(B5)}$$

which is the final expression to replace the sinc-function in the state amplitude, Eq. (A28), having now $M+1$ terms to approximate the square-shaped poling structure. For $M=0$ the expression reduces to the sinusoidal approximation with $f_1 = 4/\pi$.

[1] S. Fasel, O. Alibart, S. Tanzilli, P. Baldi, A. Beveratos, N. Gisin, and H. Zbinden, New J. Phys. **6**, 163 (2004).
[2] T. B. Pittman, B. C. Jacobs, and J. D. Franson, Opt. Commun. **246**, 545 (2004).
[3] O. Alibart, D. B. Ostrowsky, and P. Baldi, Opt. Lett. **30**, 1539 (2005).
[4] T. Jennewein, C. Simon, G. Weihs, H. Weinfurter, and A. Zeilinger, Phys. Rev. Lett. **84**, 4729 (2000).
[5] D. S. Naik, C. G. Peterson, A. G. White, A. J. Berglund, and P. G. Kwiat, Phys. Rev. Lett. **84**, 4733 (2000).
[6] G. Ribordy, J. Brendel, J.-D. Gauthier, N. Gisin, and H. Zbinden, Phys. Rev. A **63**, 012309 (2000).
[7] I. Marcikic, H. de Riedmatten, W. Tittel, H. Zbinden, and N. Gisin, Nature (London) **421**, 509 (2003).
[8] S. Tanzilli, W. Tittel, H. D. Riedmatten, H. Zbinden, P. Baldi, M. D. Micheli, D. Ostrowsky, and N. Gisin, Eur. Phys. J. D **18**, 155 (2002).
[9] W. Tittel, J. Brendel, N. Gisin, and H. Zbinden, Phys. Rev. A **59**, 4150 (1999).
[10] S. Fasel, N. Gisin, G. Ribordy, and H. Zbinden, Eur. Phys. J. D **30**, 143 (2004).
[11] G. D. Boyd and D. A. Kleinman, J. Appl. Phys. **39**, 3597 (1968).
[12] D. A. Kleinman and R. C. Miller, Phys. Rev. **148**, 302 (1966).
[13] S. Guha, F. Wu, and J. Falk, IEEE J. Quantum Electron. **18**, 907 (1982).
[14] J.-J. Zondy, Opt. Commun. **81**, 427 (1991).
[15] J.-J. Zondy, Opt. Commun. **149**, 181 (1998).
[16] C. H. Monken, P. H. Souto Ribeiro, and S. Pádua, Phys. Rev. A **57**, R2267 (1998).
[17] T. B. Pittman, D. V. Strekalov, D. N. Klyshko, M. H. Rubin, A. V. Sergienko, and Y. H. Shih, Phys. Rev. A **53**, 2804 (1996).
[18] T. Aichele, A. I. Lvovsky, and S. Schiller, Eur. Phys. J. D **18**, 237 (2002).
[19] C. Kurtsiefer, M. Oberparleiter, and H. Weinfurter, Phys. Rev. A **64**, 023802 (2001).
[20] F. A. Bovino, P. Varisco, A. M. Colla, G. Castagnoli, G. D. Giuseppe, and A. V. Sergienko, Opt. Commun. **227**, 343 (2003).
[21] S. Castelletto, I. P. Degiovanni, A. Migdall, and M. Ware, New J. Phys. **6**, 87 (2004).
[22] M. Pelton, P. Marsden, D. Ljunggren, M. Tengner, A. Karlsson, A. Fragemann, C. Canalias, and F. Laurell, Opt. Express **12**, 3573 (2004).
[23] P. G. Kwiat, E. Waks, A. G. White, I. Appelbaum, and P. H. Eberhard, Phys. Rev. A **60**, R773 (1999).
[24] D. Ljunggren, M. Tengner, M. Pelton, and P. Marsden, in *Quantum Communication, Measurement and Computing*, edited by S. M. Barnett *et al.*, AIP Conf. Proc. No. 734 (AIP, Melville, NY, 2004).
[25] C. E. Kuklewicz, M. Fiorentino, G. Messin, F. N. C. Wong, and J. H. Shapiro, Phys. Rev. A **69**, 013807 (2004).
[26] M. Fiorentino, G. Messin, C. E. Kuklewicz, F. N. C. Wong, and J. Shapiro, Phys. Rev. A **69**, 041801 (2004).
[27] T. Y. Fan, C. E. Huang, B. Q. Hu, R. C. Eckardt, Y. X. Fan, R. L. Byer, and R. S. Feigelson, Appl. Opt. **26**, 2390 (1987).
[28] K. Fradkin, A. Arie, A. Skliar, and G. Rosenman, Appl. Phys. Lett. **74**, 914 (1999).
[29] D. N. Klyshko, *Photons and Nonlinear Optics* (Gordon and Breach, New York, 1988).
[30] L. Mandel and E. Wolf, *Optical Coherence and Quantum Optics* (Cambridge University Press, Cambridge, UK, 1995).
[31] A. E. Siegman, IEEE J. Quantum Electron. **29**, 1212 (1993).
[32] A. E. Siegman, *Lasers* (University Science Books, Sausalito, 1986).
[33] P. S. K. Lee, M. P. van Exter, and J. P. Woerdman, Phys. Rev. A **70**, 043818 (2004).
[34] D. Ljunggren, M. Tengner, P. Marsden, and M. Pelton (to be published).